Joule

CellPress

Article

Quantum-Dot-Derived Catalysts for CO_2 Reduction Reaction

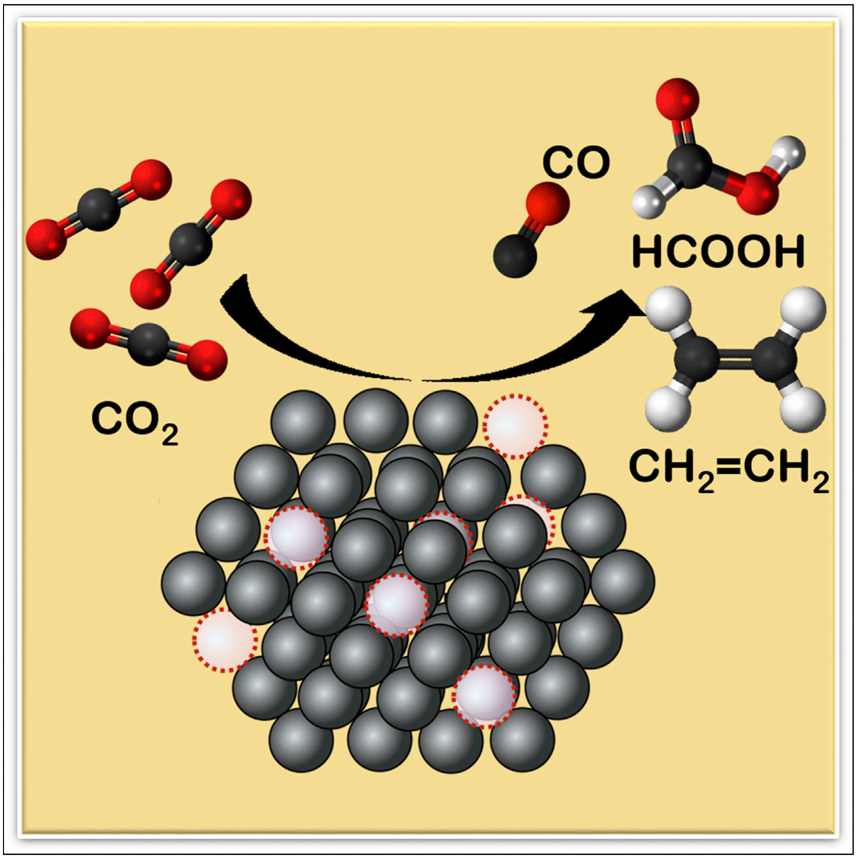

A high density of homogeneously dispersed atomic defects has long been believed to be a promising strategy for improving catalytic activity. Taking the defective nature of quantum dots, Liu et al. synthesize vacancy-rich metal nanocrystals through *in situ* electrochemical reduction of quantum dots. This maximizes the density and stability of vacancies in metallic nanocrystals and achieves record current densities with high faradic efficiencies in the electrosynthesis of formate, carbon monoxide, and ethylene at low applied potentials.

Min Liu, Mengxia Liu, Xiaoming Wang, ..., Tsun-Kong Sham, Bing-Joe Hwang, Edward H. Sargent

minliu@csu.edu.cn (M.L.)
bjh@mail.ntust.edu.tw (B.-J.H.)
ted.sargent@utoronto.ca (E.H.S.)

HIGHLIGHTS

QDDCs were synthesized through *in situ* electrochemical reduction

QDDCs maximize the density and stability of vacancies in metallic nanocrystals

QDDCs produce a local atomic and electronic structure that enhances CO_2RR performances

QDDCs provide further avenues to catalyst design and optimization

Liu et al., Joule 3, 1–16
July 17, 2019
https://doi.org/10.1016/j.joule.2019.05.010

Please cite this article in press as: Liu et al., Quantum-Dot-Derived Catalysts for CO_2 Reduction Reaction, Joule (2019), https://doi.org/10.1016/j.joule.2019.05.010

Joule

CellPress

Article

Quantum-Dot-Derived Catalysts for CO_2 Reduction Reaction

Min Liu,[1,2,3,12,*] Mengxia Liu,[2,12] Xiaoming Wang,[4,12] Sergey M. Kozlov,[5] Zhen Cao,[5] Phil De Luna,[6] Hongmei Li,[1] Xiaoqing Qiu,[3] Kang Liu,[1] Junhua Hu,[7] Chuankun Jia,[8] Peng Wang,[1] Huimin Zhou,[1] Jun He,[1] Miao Zhong,[2] Xinzheng Lan,[2] Yansong Zhou,[2] Zhiqiang Wang,[9] Jun Li,[9] Ali Seifitokaldani,[2] Cao Thang Dinh,[2] Hongyan Liang,[2] Chengqin Zou,[2] Daliang Zhang,[10] Yang Yang,[10] Ting-Shan Chan,[11] Yu Han,[10] Luigi Cavallo,[5] Tsun-Kong Sham,[9] Bing-Joe Hwang,[4,11,*] and Edward H. Sargent[2,13,*]

SUMMARY

Defect sites are often proposed as key active sites in the design of catalysts. A promising strategy for improving activity is to achieve a high density of homogeneously dispersed atomic defects; however, this is seldom accomplished in metals. We hypothesize that vacancy-rich catalysts could be obtained through the synthesis of quantum dots (QDs) and their electrochemical reduction during the CO_2 reduction reaction (CO_2RR). Here, we report that QD-derived catalysts (QDDCs) with up to 20 vol % vacancies achieve record current densities of 16, 19, and 25 mAcm^{-2} with high faradic efficiencies in the electrosynthesis of formate, carbon monoxide, and ethylene at low potentials of –0.2, –0.3, and –0.9 V versus reversible hydrogen electrode (RHE), respectively. The materials are stable after 80 hr of CO_2RR. These CO_2RR performances in aqueous solution surpass those of previously reported catalysts by 2×. Together, X-ray absorption spectroscopy and computational studies reveal that the vacancies produce a local atomic and electronic structure that enhances CO_2RR.

INTRODUCTION

The electroreduction of CO_2 to valuable carbon-based products and feedstocks provides an attractive paradigm for the storage of intermittent renewable electricity and thus contributes toward reducing net greenhouse gas emissions.[1–8] Although the CO_2 reduction reaction (CO_2RR) has reached low activation overpotentials and increased faradic efficiencies (FEs) via the tuning of catalyst morphologies,[1,8–11] manipulation of oxidation states,[5,8,12,13] and introduction of dopants,[14–16] CO_2 electroreduction still requires further efforts toward high catalytic activity, selectivity, and durability.

Quantum dots (QDs), emerging solution-processed materials that have a small size, high surface-to-volume ratio, and high monodispersity, are interesting but also challenging materials for optoelectronics in light of their potential to have high atomic vacancy densities.[17–20] In catalysis, though, defect sites are often proposed as key active sites because they can lower the energy barrier for the electrosynthesis of desired chemical products.[21–27] This suggests a general design principle for developing efficient CO_2RR catalysts with high activity and selectivity with QDs.

Here, we report the synthesis of QD-derived catalysts (QDDCs) for CO_2RR through the *in situ* electrochemical reduction of QDs in CO_2-saturated 0.5 M $KHCO_3$ electrolyte. This maximizes the density and stability of vacancies in metallic nanocrystals.

Context & Scale

Using renewable electricity to convert CO_2 into value-added carbon-based products and feedstocks simultaneously addresses the needs for storage of intermittent renewable energy sources and reduces greenhouse gas emissions. We report record current densities with high faradic efficiencies in the electrosynthesis of formate, carbon monoxide, and ethylene at the low applied potentials through the synthesis of quantum-dot-derived catalysts (QDDCs). The QDDCs maximize the density and stability of vacancies in metallic nanocrystals and thus the catalytic activity and stability. The catalysts show excellent stability without deactivation after more than 80 h of operation.

Please cite this article in press as: Liu et al., Quantum-Dot-Derived Catalysts for CO_2 Reduction Reaction, Joule (2019), https://doi.org/10.1016/j.joule.2019.05.010

The synthesis thereby produces a local atomic and electronic structure that drastically enhances CO_2RR performances.

RESULTS AND DISCUSSION

We first used computational stimulations to investigate the impact of metal atomic vacancies on CO_2RR. We obtained Gibbs free energy (ΔG) diagrams by using density functional theory (DFT) calculations on Pb and Au surfaces with and without vacancies (Figures 1A–1F, S1, and S2). The results showed that CO_2RR overpotentials decreased on a variety of metal facets when vacancies were present. In particular, overpotentials were decreased by ~90%, e.g., from 0.169 to 0.017 V, on Pb (110) and by ~25% on Au (100) when vacancies were incorporated. This improved activity can also be depicted as a volcano-like dependency for the CO_2RR onset potential (Figure S3): the presence of vacancies weakens the binding strength of intermediate HCOO* on the facets, lowering the energetic barrier and determining the rate of reaction.

To study the stability of vacancy generation in these systems, we also obtained the formation energies associated with vacancies on metal, metal sulfide, and metal oxide slabs of gold (Au), lead (Pb), and copper (Cu) (Figures 1G and S4 and Table S1). The results indicated that metal sulfides favor vacancy generation. To investigate the effect of vacancies on the electronic structure of Pb and Au nanoparticles (NPs), we examined both pristine and defective ~3 nm Pb_{459} and Au_{459}. We computationally generated the defective structures by removing 20% of the atoms at random. The results showed that the defects localized the electron density around the surface atoms and subsequently altered their catalytic activity in CO_2RR (Figures 1H–1K). Together, these results suggest that metal sulfides are a promising platform for the synthesis of vacancy-rich nanocrystals: they offer the possibility of localizing electronic structure and thereby decreasing the barrier to CO_2RR.

To verify the computational predictions, we pursued the synthesis of vacancy-rich metallic nanocrystals for CO_2RR through the *in situ* electrochemical reduction of QDs in CO_2-saturated 0.5 M $KHCO_3$ electrolyte (Figure 2A). We began with metal chalcogenide QDs, such as lead sulfide (PbS) and gold sulfide (Au_2S) QDs (Figures S5–S7), from which we obtained QDDCs. Transmission electron microscopy (TEM) revealed that the QDDCs retained the particle size of the original QDs and that vacancies were progressively generated in the QDs as sulfur atoms were liberated (Figures S8 and S9). X-ray diffraction (XRD) spectra showed that QDDCs consisted of metallic Pb and Au (Figure S10). X-ray photoelectron spectroscopy (XPS) and X-ray absorption near-edge structure (XANES) spectra showed features characteristic of Pb^0 and Au^0, but no sulfur (Figures S11–S13).

We then sought to compare the density of vacancies with that of controls. High-angle annular dark-field scanning transmission electron microscopy (HAADF-STEM) images showed well-aligned atoms with obvious vacancies in Pb (Figures 2B–2D) and Au (Figures 2I–2K) QDDCs. The corresponding three-dimensional topographic images and linear integrated pixel intensities confirmed that vacancies resided in Pb (Figures 2E–2J and S14) and Au (Figures 2L–2N and S15) QDDCs. We found that the density of vacancies increased as NP size decreased from ~5% for 5 nm dots to ~10% for 4 nm dots and reached ~20% for 3 nm dots (Tables S2 and S3). Positron annihilation spectrometry results further confirmed these trends. In comparison, in controls based on metal NPs (Pb and Au NPs, size ~3 nm) and commercial metal particles (Pb and Au particles, size ~ 200 nm), vacancies were not observed after similar reduction treatments (Figures S16–S19).

[1]Institute of Super-microstructure and Ultrafast Process in Advanced Materials, School of Physics and Electronics, Central South University, 932 South Lushan Road, Changsha, Hunan 410083, China

[2]Department of Electrical and Computer Engineering, University of Toronto, 35 St. George Street, Toronto, ON M5S 1A4, Canada

[3]Hunan provincial Key Laboratory of Chemical Powersources, State Key Laboratory of Powder Metallurgy, College of Chemistry and Chemical Engineering, Central South University, 932 South Lushan Road, Changsha, Hunan 410083, China

[4]Department of Chemical Engineering, National Taiwan University of Science and Technology, 43, Section 4, Keelung Road, Taipei City, 106, Taiwan

[5]KAUST Catalysis Center, King Abdullah University of Science and Technology (KAUST), Thuwal 23955-6900, Saudi Arabia

[6]Department of Materials Science and Engineering, University of Toronto, 27 King's College Circle, Toronto, ON M5S 1A1, Canada

[7]School of Materials Science and Engineering, Zhengzhou University, Zhengzhou 450001, China

[8]College of Materials Science and Engineering, Changsha University of Science & Technology, Changsha 410114, China

[9]Department of Chemistry, University of Western Ontario, 1151 Richmond Street, London, ON N6A 5B7, Canada

[10]Advanced Membranes and Porous Materials Center, King Abdullah University of Science and Technology (KAUST), Thuwal 23955-6900, Saudi Arabia

[11]National Synchrotron Radiation Research Center, 101 Hsin Ann Road, Hsinchu Science Park, Hsinchu, 300, Taiwan

[12]These authors contributed equally

[13]Lead Contact

*Correspondence: minliu@csu.edu.cn (M.L.), bjh@mail.ntust.edu.tw (B.-J.H.), ted.sargent@utoronto.ca (E.H.S.)

https://doi.org/10.1016/j.joule.2019.05.010

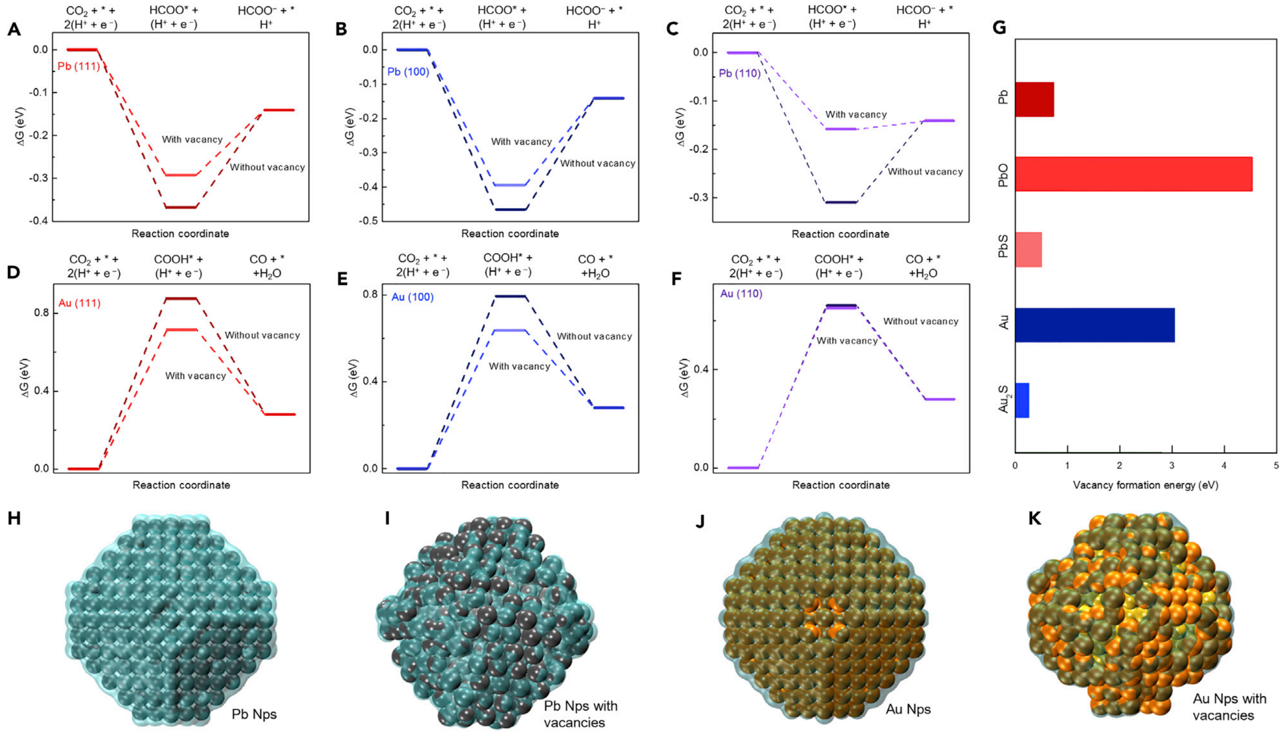

Figure 1. Thermodynamic Energy Profiles for the CO_2RR, Vacancy Formation Energies, and Electronic Structures on Pb and Au NPs

(A–C) Gibbs free energy (ΔG) diagrams of the electrochemical reduction of CO_2 to formate on pristine and vacancy-containing Pb(111) (A), Pb(100) (B), and Pb(110) (C) facets.

(D–F) ΔG diagrams of the electrochemical reduction of CO_2 to CO on pristine and vacancy-containing Au(111) (D), Au(100) (E), and Au(110) (F) facets.

(G) Vacancy formation energies for Pb and Au metal, oxide, and sulfide.

(H–K) Electronic structures of Pb and Au NPs with and without vacancies.

To elucidate the vacancy generation process, we carried out *in situ* Raman and *in situ* X-ray absorption spectroscopy (XAS) studies under CO_2RR conditions (Figures 3, S9, and S20–S24). XANES and Raman spectra showed that the features of sulfide decreased gradually over the course of the reaction (Figures S9 and S20). After ~90 min of operation in CO_2-saturated 0.5 M $KHCO_3$ at −0.2 V versus reversible hydrogen electrode (RHE), the features of sulfide had completely disappeared: this result suggests that the QDs were completely reduced to a metallic state (Figure S21). By evaluating the results of extended X-ray absorption fine structure (EXAFS), we found that Au-S bonding decreased over the course of the reaction and became imperceptible over ~90 min of operation (Figures 3A and 3B). The Au-Au distance decreased from the initial Au_2S during catalytic operation and reached a steady value after ~90 min of operation (Figure 3C and Table S4). The Au-Au coordination number (CN) increased from ~4.4 in the initial Au_2S to a steady value of ~9.0 after ~90 min of operation (Figure 3C and Table S4). These results indicate more Au-Au bonding during desulfurization accompanied by metal formation. Notably, the stable Au-Au CN was much smaller than those in Au foil and Au NPs (Figures 3C and 3F), suggesting the formation of undercoordinated sites from atomic vacancies.

We then proceeded to study the atomic and electronic structures of the QDDCs with different sizes and to compare them with those of ~3 nm metal NPs (Figures 3D–3I and S22 and Tables S5 and S6). For the non-vacancy samples, the metal-metal (Pb-Pb and Au-Au) bonding distance and CN of metal NPs each decreased with the smaller particle size, consistent with previous reports.[28,29] In contrast, for

Please cite this article in press as: Liu et al., Quantum-Dot-Derived Catalysts for CO_2 Reduction Reaction, Joule (2019), https://doi.org/10.1016/j.joule.2019.05.010

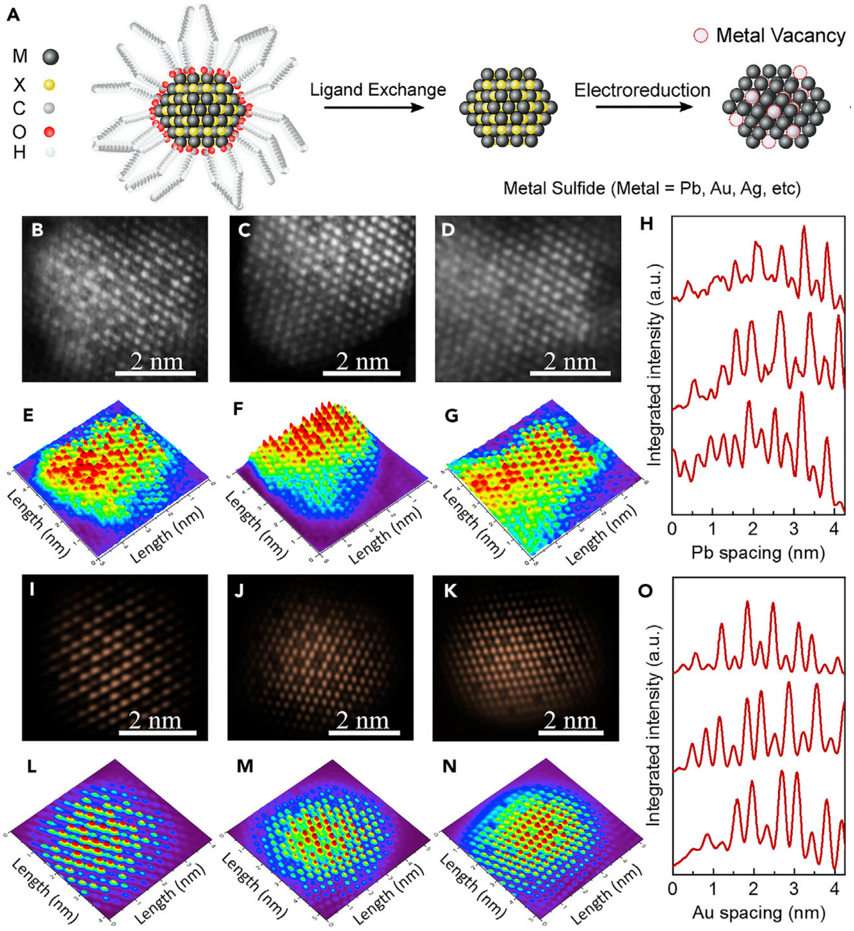

Figure 2. Generation Schematic and High-Resolution HAADF-STEM Images for Vacancy-Rich Pb and Au QDDCs

(A) Schematic of the process for preparing vacancy-rich QDDCs. The organic ligands were first removed by a ligand-exchange process, and the obtained QDs were electrochemically reduced to create vacancy-rich QDDCs.

(B–D) HAADF-STEM images of Pb QDDCs with particle sizes of 3 nm (B), 4 nm (E), and 5 nm (D).

(E–G) The corresponding three-dimensional topographic images for the HAADF-STEM images in (B)–(D). Color was applied to enhance the contrast.

(H) The integrated pixel intensities of Pb QDDCs. The peaks represent atom locations. Vacancies can be observed from the relatively weak peak intensities.

(I–K) HAADF-STEM images of Au QDDCs with particle sizes of 3 nm (I), 4 nm (J), and 5 nm (K).

(L–N) The corresponding three-dimensional topographic images for HAADF-STEM images in (I)–(K). Color was applied to enhance the contrast.

(O) The integrated pixel intensities of Au QDDCs. The peaks represent atom locations. Vacancies can be observed from the relatively weak peak intensities.

vacancy-rich QDDC samples with similar particle size, the Pb-Pb and Au-Au bonding distances followed the opposite trend: instead of decreasing with smaller size, the average bond distance within QDDCs increased appreciably. We associate this with the increased density of vacancies and note that it is consistent with a major role of vacancies in influencing atomic structure.[30] This is evidence of local atomic and electronic structure modification.

To evaluate the stability of vacancies, we measured EXAFS *in situ* as a function of increasingly reducing potential (Figures S23 and S24 and Tables S5 and S6). The enlarged

Please cite this article in press as: Liu et al., Quantum-Dot-Derived Catalysts for CO_2 Reduction Reaction, Joule (2019), https://doi.org/10.1016/j.joule.2019.05.010

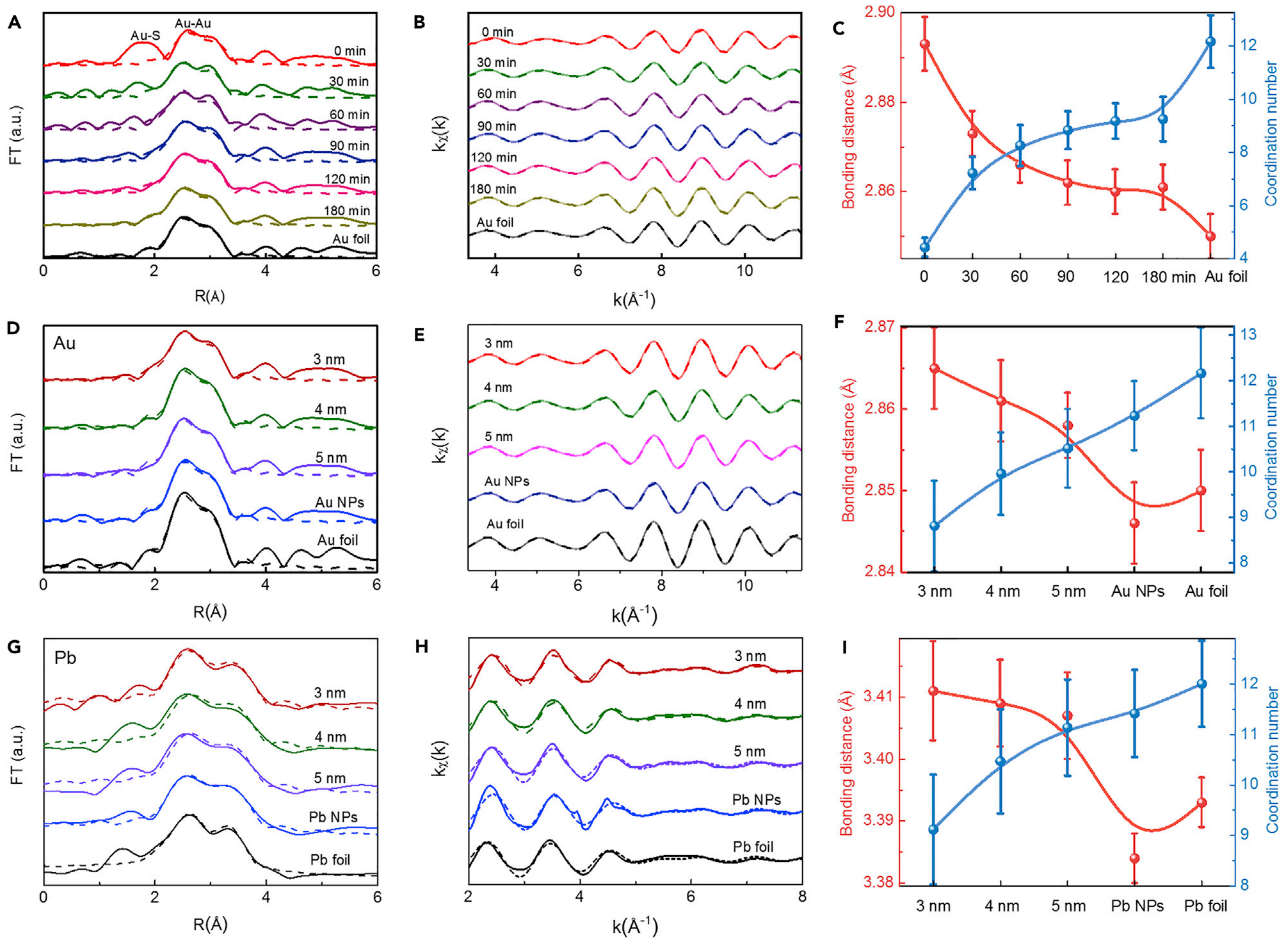

Figure 3. ***In Situ*** **X-Ray Absorption Spectra of Pb and Au QDDCs**

(A and B) *In situ* Au L_3-edge EXAFS spectra and their corresponding fitting curves in the R space (A) and K space (B) for Au QDDCs with different reaction times, Au NPs, and Au foil.

(C) Bonding distances and CNs obtained from EXAFS fitting results for Au QDDCs with different reaction times.

(D and E) Au L_3-edge EXAFS spectra and their corresponding fitting curves in the R space (D) and K space (E) for completely reduced Au QDDCs with different sizes, Au NPs and Au foil.

(F) Bonding distances and CNs obtained from EXAFS fitting results for Au QDDCs with different sizes, Au NPs, and Au foil.

(G and H) Pb L_3-edge EXAFS spectra and their corresponding fitting curves in the R space (G) and K space (H) for Pb QDDCs with different sizes, Pb NPs, and Pb foil.

(I) Bonding distances and CNs obtained from EXAFS fitting results for Pb QDDCs with different sizes, Pb NPs, and Pb foil.

Error bars in (C), (F), and (I) were aroused by nonlinear least-squares algorithm curve fitting in the *r* space range.

bonding distances and decreased CNs were similar across potentials, indicating an identical local atomic structure and a high stability of vacancies in the 3 nm QDDCs.

As a control, we explored the use of metal sulfide microparticles and found that they failed to be completely reduced to metal even under −1.0 V versus RHE for 10 h of operation (Figure S25). This result highlights the necessity of using QD NPs to access the proper size regime to facilitate metal atomic vacancies.

To challenge our prediction of enhanced CO_2RR with vacancy-rich QDDCs, we compared their CO_2RR activity with that of metal NPs in CO_2-saturated 0.5 M $KHCO_3$ electrolyte (Figures S26–S28). Linear sweep voltammetry (LSV) curves taken from 0.4 to −1.0 V versus RHE showed that current densities of QDDCs notably

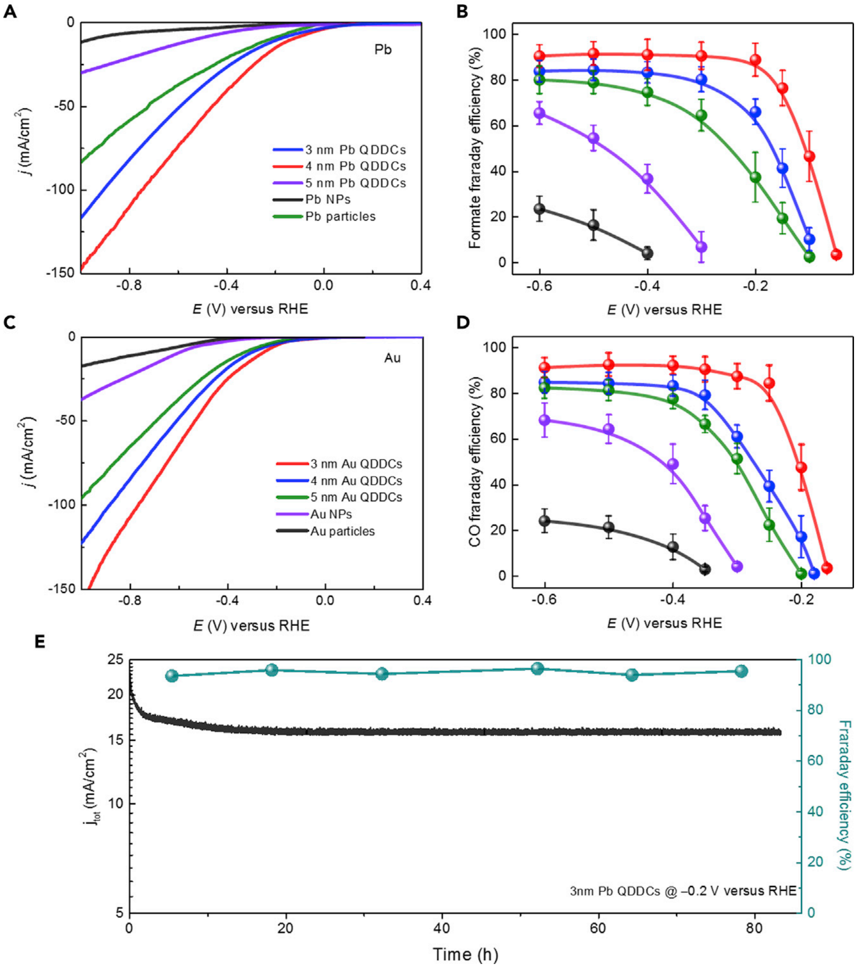

Figure 4. CO_2 Reduction Performance on Pb and Au QDDCs

(A) Current-voltage curves on Pb QDDCs, Pb NPs, and Pb particles obtained from LSV scans. The scan rate was 10 mV/s.

(B) Formate FEs on Pb QDDCs, Pb NPs, and Pb particles at different applied potentials.

(C) Current-voltage curves on Au QDDCs, Au NPs, and Au particles obtained from LSV scans. Scan rate, 10 mV/s.

(D) CO FEs on Au QDDCs, Au NPs, and Au pentagonal NPs at different applied potentials.

(E) CO_2 reduction activity for Pb QDDCs needles at −0.2 V versus RHE. The total current density (left axis) versus time and formate FE (right axis) versus time indicate high stability and selectivity for CO_2RR. The error bars, ±5, were calculated with at least three independent experiments.

exceeded those of controls and improved as vacancy densities increased (Figures 4A and 4C). Notably, 3 nm Pb and Au QDDCs, which possess the largest densities of vacancies, exhibited record stable geometric current densities (*j*) of ~16 and ~19 mA cm^{-2}, respectively, at low potentials of −0.2 and −0.3 V versus RHE, respectively, for over 80 h of continuous reaction (Figures 4E, S27, and S28 and Table 1).[5,31–33] These current density values are 30× and 200× larger than the current densities for NPs and particles, respectively. This activity could be partly attributed to the increased propensity for CO_2 molecules to adsorb onto the surface of the QDDCs, as evidenced by CO_2 gas adsorption experiments (Figure S29).

Quantification of CO_2RR products via ^{1}H nuclear magnetic resonance (NMR) (Figure S30) and gas chromatography (Figure S31) revealed that 3 nm QDDCs had the

Please cite this article in press as: Liu et al., Quantum-Dot-Derived Catalysts for CO_2 Reduction Reaction, Joule (2019), https://doi.org/10.1016/j.joule.2019.05.010

Table 1. Comparison of CO_2RR Performances on QDDCs and Controls

Catalyst	Electrolyte	Loading Amount (mg/cm^2)	j (mA/cm^2)	FE	Onset Over-potential (η)	Tafel Slope (mV dec^{-1})	Reference
Partially oxidized Co	0.1 M Na_2SO_4	0.27	10 (-0.24 V_{RHE})	90%	70 mV	44	Gao et al.[5]
Pd needles	0.5 M $KHCO_3$	–	10 (-0.2 V_{RHE})	90%	70 mV	–	Liu et al.[1]
Oxide-derived Pb	0.5 M KHCO3	–	1 (-1.0 V_{RHE})	95%	200 mV	83	Lee and Kanan[31]
Au nanowire	0.5 M $KHCO_3$	–	1 (-0.3 V_{RHE})	80%	90 mV	–	Zu et al.[9]
Au needles	0.5 M $KHCO_3$	–	8 (-0.3 V_{RHE})	90%	70 mV	36	Lu et al.[1]
Nanoporous Ag	0.5 M $KHCO_3$	–	4 (-0.4 V_{RHE})	80%	100 mV	58	Lu et al.[10]
Plasma-treated Cu	0.1 M $KHCO_3$	–	10 (-0.9 V_{RHE})	60%	550 mV	–	Mistry et al.[13]
Pb QDDCs	0.5 M $KHCO_3$	0.18	16 (-0.2 V_{RHE})	95%	40 mV	36	this work
Au QDDCs	0.5 M $KHCO_3$	0.19	19 (-0.3 V_{RHE})	95%	50 mV	33	this work
Ag QDDCs	0.5 M $KHCO_3$	0.18	16 (-0.3 V_{RHE})	95%	70 mV	38	this work
Cu QDDCs	0.5 M $KHCO_3$	0.16	25 (-0.9 V_{RHE})	53%	420 mV	50	this work

highest FE—a value equal to ~95%—among the five classes of samples that produced formate and CO (Figures 4B and 4D). No obvious changes were observed in morphology or surface state after long-term CO_2RR, consistent with the fact that QDDCs are stable under electrocatalytic conditions (Figures S32 and S33). Notably, the onset of CO_2RR occurred at an exceptionally low potential of -0.05 V ($\eta_{formate} = 0.04$ V) and -0.16 V ($\eta_{CO} = 0.05$ V) versus RHE,[5] and the FE for formate and CO generation was measured to be ~5% on 3 nm Pb and Au QDDCs at this potential, respectively (Figures 4B and 4D). These onset potentials are significantly lower than the values when metal NPs are used.

In contrast, no significant CO_2 reduction was observed for Pb or Au NPs or particles at applied potentials closer to -0.3 or -0.4 V versus RHE, respectively (Figures 4B and 4D). The activity and stability decreased rapidly in the case of these control samples (Figures S27 and S28). The dramatic loss in activity observed in the case of NPs and particles suggests that atomic vacancies play a vital role in the interaction with CO_2 molecules (Figure S29) and sustained high activity of QDDCs.

Next, to elucidate the origin of improved catalytic performance, we then investigated the electrochemical surface area (ECSA) of the catalysts and compared their ECSA-normalized partial current densities for formate ($j_{formate}$) and CO (j_{CO}) production with the applied potential for the electrodes (Figures S34–S38 and Tables S10 and S11). Notably, both ECSA and Brunauer-Emmett-Teller (BET) surface-area analyses showed that Pb and Au QDDCs had surface areas identical to those of metal NPs, yet they showed 30× and 40× higher catalytic activities at -0.2 and -0.3 V versus RHE, respectively (Figures S36 and S37). These data indicate high intrinsic activity arising from vacancy active sites.

To explore the kinetics of CO_2RR on the QDDCs, we carried out Tafel analysis (Figure S39). ECSA-corrected Tafel slopes for formate and CO production using metal NPs and particles were ~100 and ~120 mV dec^{-1}, respectively, agreeing well with prior reports (103 and 150 mV dec^{-1}, respectively) and indicating the involvement of a rate-limiting one-electron ($1e^-$) process.[1,5,34] Generally, during two-electron CO_2RR, the first $1e^-$ step of converting CO_2 to COOH* or $CO_2^{\cdot -}$ intermediates is rate determining for the combined process.[1,5,34,35] In comparison, QDDCs show much lower Tafel slopes of ~35 mV dec^{-1} for 3 nm size, indicating a fast pre-equilibrium involving a $1e^-$ transfer to form COOH* or $CO_2^{\cdot -}$ intermediates.[1,5] These

Please cite this article in press as: Liu et al., Quantum-Dot-Derived Catalysts for CO_2 Reduction Reaction, Joule (2019), https://doi.org/10.1016/j.joule.2019.05.010

results are in agreement with the theoretical calculations above, as well as the CO_2 gas adsorption experiments, which each also suggest higher intrinsic CO_2RR activities for QDDCs.

Next, we investigated electrochemical impedance spectroscopy (EIS) for QDDCs and controls to probe charge-transfer processes occurring at electrode-solution interfaces (Figure S40 and Tables S12 and S13). The smaller semicircle sizes of the Nyquist plots for QDDCs confirmed the acceleration of charge-transfer processes in QDDCs. This provides the evidence of improved kinetics of charge transfer on QDDCs, facilitating the first pre-equilibrium step involving $1e^-$ transfer.

We further studied the effect of temperature on the performance of the catalysts to assess the kinetic barriers of reaction (Figures S41 and S42). CO_2RR proceeds more rapidly at elevated temperatures, reflecting the exponential temperature dependence of the chemical reaction constant.[1,36] The electrochemical activation energies were extracted from the slopes of the Arrhenius plots and agreed well with previously reported values (Figures S41 and S42 and Tables S14 and S15).[1,37,38] We found that the experimental energy barriers decreased from particles to QDDCs and reached the lowest value of ~20 kJ mol^{-1} for 3 nm Pb and Au QDDCs. These results again indicate that vacancies improve the kinetics of CO_2RR.

To investigate the breadth of applicability of the QDDC concept, we prepared silver (Ag) and Cu QDDCs and studied their CO_2RR performance (Figures S43–S51). As indicated by XRD, XPS, and XAS, the final (post-CO_2RR) QDDCs did consist of metallic Ag and Cu (Figures S43 and S49). TEM and XAS revealed that controlling the particle size can be used to adjust the density of vacancies (Figures S44–S46, S50, and S51). The Ag and Cu QDDCs exhibiting the highest ratio of vacancies exhibited enhanced CO_2-to-CO and CO_2-to-ethylene conversion relative to that of Ag and Cu nanostructures and particles (Table 1).[9,10,13]

This work features the modulation of atomic and electronic structure arising from the incorporation of vacancies in the metal NPs and highlights the benefits of the approach in CO_2RR. Vacancy-rich metal catalysts provide further avenues to catalyst design and optimization. The synthesis of these metals from metal chalcogenide NPs offers a promising new degree of freedom in the implementation of this concept.

EXPERIMENTAL PROCEDURES

Computational Details

We used the Vienna Ab initio Simulation package (VASP)[39] for DFT calculations with the Perdew-Burke-Ernzerhof (PBE)[40] exchange-correlation functional augmented with semi-empirical Grimme D3 corrections for dispersive interactions.[41] Valence electrons were described with a 400 eV plane-wave basis set, and their interaction with core electrons was treated with the projected augmented wave (PAW) technique.[42] The Gaussian smearing of 0.1 eV was applied to the occupation of electronic eigenstates. Slab calculations were performed with a 3 × 3 × 1 k-point mesh.

Geometry optimization was performed until the forces on atoms became less than 0.1 eV/nm with all atoms relaxed. We considered the following five-layer slabs with experimental lattice parameters[43] of Pb and Au: a 1.40 × 1.40 nm and 1.15 × 1.15 nm p(4 × 4) slab for the (100) surface, a 1.40 × 1.48 nm

Please cite this article in press as: Liu et al., Quantum-Dot-Derived Catalysts for CO_2 Reduction Reaction, Joule (2019), https://doi.org/10.1016/j.joule.2019.05.010

and 1.15 × 1.22 nm p(4 × 3) slab for the (110) surface, a 1.40 × 1.40 nm and 1.15 × 1.15 nm p(4 × 4) slab for the (111) surface, and 0.88 × 1.08 nm and 1.41 × 0.86 nm p(1 × 3) and p(2 × 3) slabs for the (211) surface. The vacuum separation between adjacent slabs was higher than 1 nm.

The metal clusters were presented with a cluster containing 459 Pb or Au atoms. Thereafter, we removed 20% of the surface atoms from the cluster to generate highly defective clusters. The obtained metal clusters were optimized by the same algorithm described above with a 1 × 1 × 1 k-point mesh. Thereafter, we chose the electrons in the energy levels within 0.1 eV lower than the fermi level to plot the electron density.

To calculate the contribution of molecular vibrations to Gibbs free energies at 298 K (including zero-point energy corrections), we calculated vibrations of the involved species by applying finite displacements of 3 pm to H, C, and O atoms, whereas positions of metal atoms remained fixed.

Computational Electrochemistry

The CO_2RR mechanism considered for formate production on Pb catalysts is $CO_2^* \xrightarrow{+H^+ +e^-} HCOO^* \xrightarrow{+e^-} HCOO^{-,sol}$ where sol stands for solvated species. In line with a previous study,[44] CO_2^* (which is physisorbed on Pb), CO_2^{sol}, and CO_2^{gas} are considered to be equilibrated with each other, i.e., to have equal Gibbs free energies, $G(CO_2^*) = G(CO_2^{sol}) = G(CO_2^{gas})$. The Gibbs energy of the product, $HCOO^{-,sol}$, can be derived at a given pH from the Gibbs energy of $HCOOH^{sol}$ with the experimental pK_a value $G(HCOO^{-,sol}) = G(HCOOH^{sol}) - k_BT \times \ln 10 \times (pH - pK_a) = G(HCOOH^{sol}) -$ 0.20 eV at experimental pH = 7.2 and pK_a = 3.77. In turn, $HCOOH^{sol}$ is assumed to be equilibrated with $HCOOH^{gas}$. The Gibbs energies of gas-phase species were calculated by a standard thermochemical approach within the ideal gas approximation at fugacities $f(CO_2^{gas}) = 101,325$ Pa and $f(HCOOH^{gas}) = 2$ Pa, chosen to be in line with previous computational studies of CO_2RR.[44] Free energies of protons and electrons, $G(H^{+,sol})$ and $G(e^-)$, are described according to the computational hydrogen electrode approach.[45] At the given fugacities and the given pH, the reaction free energy $\Delta G(CO_2^{gas} + H^+ + 2e^- \rightarrow HCOO^{-,sol})$ is calculated to be 0.109 eV at the RHE potential. That is, the calculated equilibrium potential for this reaction is −0.055V versus RHE, which compares nicely to the experimental value of −0.05 V versus RHE. We calculated the HCOO* intermediate on all possible high-symmetry adsorption sites on pristine Pb surfaces. On surfaces with vacancies, only high-symmetry sites directly involving vacancies were considered. The obtained configurations with lowest energies are displayed in Figure S1.

For CO_2 reduction to CO on Au, we considered the following mechanism: $CO_2^* \xrightarrow{+H^+ +e^-} COOH^* \xrightarrow{+H^+ +e^- -H_2O} CO^* \rightarrow CO^{gas}$. Gibbs energies of CO_2, H^+, and e^- were calculated as explained before. Gibbs energies of CO and H_2O were calculated with the ideal gas approximation at fugacities $f(CO^{gas}) = 5,562$ Pa and $f(H_2O) = 3,534$ Pa, chosen to be in line with Peterson et al.[44] The latter value corresponds to the fugacity of water vapors in equilibrium with liquid water at room temperature. The calculated structures of COOH* intermediates on Au surfaces are displayed in Figure S2. At the given fugacities, the reaction free energy $\Delta G(CO_2^{gas} + 2H^+ + 2e^- \rightarrow CO^{gas} + H_2O)$ is calculated to be endothermic by 0.68 eV. Thus, its equilibrium thermodynamic potential is −0.34 V versus RHE, whereas the experimental value is −0.11 V versus RHE.

Please cite this article in press as: Liu et al., Quantum-Dot-Derived Catalysts for CO_2 Reduction Reaction, Joule (2019), https://doi.org/10.1016/j.joule.2019.05.010

Corrections regarding to the C-O bond in the reactions were applied to our computational results.[46] As expected, these corrections improved the reaction energy and the equilibrium potential for $CO_2 \rightarrow CO$ reduction on Au but made the respective values a little bit worse for the $CO_2 \rightarrow HCOO^-$ reaction on Pb. Interestingly, these corrections only slightly affected the calculated overpotentials of the $CO_2 \rightarrow HCOO^-$ reduction and had no effect on the overpotentials of the $CO_2 \rightarrow CO$ reaction.

Calculations of Vacancy Formation Energy

To provide an approximation of thermodynamic stability of the atomic vacancies, we calculated the vacancy formation energies on metal, metal sulfide, and metal oxide slabs of Au, Au_2O_3, Au_2S, Cu, CuO, CuS, Pb, PbO, and PbS. DFT calculations were performed with the VASP. The PBE generalized gradient approximation exchange-correlation functional was used. All-electron frozen-core PAW pseudopotentials with a Blöchl plane-wave basis set were used with a cutoff energy of 500 eV, a fermi smearing width of 0.1 eV, and dipole corrections. Monkhorst-Pack mesh was used for k-point sampling; 6 × 6 × 6 k-points were sampled for the optimization of all bulk structures, and 5 × 5 × 1 k-points were sampled for all slabs. The (111) surface slabs were modeled to be 3 × 3 × 3 repeating units with a vacuum space of at least 10 Å perpendicular to the surface. The (111) surface facet was chosen across all materials to provide a consistent treatment of the surface. Structural and unit-cell optimizations were performed with the Broyden-Fletcher-Goldfarb-Shanno algorithm until the maximum structural optimization cutoff was set to 0.02 eV/atom.

The vacancy formation energy is the energy difference between a slab with an atomic vacancy and a pristine slab and can be written as follows,

$$E_{F(\text{vacancy})} = E_{\text{slab}-x} - (E_{\text{slab}} + E_x), \qquad \text{(Equation 1)}$$

where $E_{F(\text{vacancy})}$ is the vacancy formation energy, $E_{\text{slab-x}}$ is the energy of the slab with an atomic vacancy, E_{Slab} is the energy of the slab without an atomic vacancy, and E_x is the energy of the bulk pure metal divided by the formula unit of the unit cell.

We found that for elements Au, Cu, and Pb, the $E_{F(\text{vacancy})}$ was lowest for the metal sulfide structures. It should be noted that the Au_2O_3 slab with an atomic vacancy failed to converge, suggesting that binding of an Au atom in the Au_2O_3 surface lattice is very high, and thus the formation of an atomic vacancy on gold oxide is very unfavorable.

QD Synthesis and Ligand Exchange

Oleic-acid-capped PbS QDs were synthesized according to previously reported methods.[47] We synthesized copper(I) sulfide QDs by introducing the Cu precursor solution (4.3 mmol copper(II) acetylacetonate and 41 mmol oleic acid heated to 110°C) into the sulfur solution (ammonium diethyldithiocarbamate, 1-dodecanethiol (10 mL), and oleic acid heated to 180°C under argon). We controlled the QD size by varying the Cu-to-S-precursor ratio. 5 nm CQDs were synthesized with a Cu:S ratio of 1:1. For 3 nm CQDs, a ratio of 5:1 was used.[48] The synthesis of silver sulfide QDs included 0.3 mmol silver nitrate and 7 mmol 3-mercaptopropionic acid mix with 4.5 mL ethylene glycol. The reaction mixture was pumped for 10 min under vacuum before being refilled with dry argon. The mixture was then heated to 145°C for the CQD growth. After some time, the reaction mixture turned from clear to dark. We controlled CQD size by modulating the reaction time. We quenched the growth by cooling the reaction mixture in ice water.[49] For gold(III) sulfide QD synthesis, we dissolved sulfur (15.40 mg, 0.481 mmol) in 12 mL decalin in a Suslick reaction vessel by stirring it on a magnetic stirrer for 10 min. We added gold acetate, $Au(CH_3COO)_3$ (100 mg, 0.267 mmol), and stirred the slurry for another 10 min to obtain better homogenization. The mixture was outgassed with nitrogen for 15 min. Then the slurry was irradiated for 2 h under nitrogen with ultrasound in a cooling bath with a constant temperature of 0°C.[50] The solution-phase ligand-exchange process was carried out in a test tube in air with lead iodide and ammonium acetate as precursors.[17] Lead iodide (0.1 M) and NH_4Ac (0.04 M) were pre-dissolved in dimethylformamide (DMF). A 5 mL amount of QD octane solution (10 mg/mL) was added to a 5 mL of precursor solution. These were mixed vigorously for 1–2 min until the CQDs completely transferred to the DMF phase. The DMF solution was washed three times with octane. After ligand exchange, carbon (Vulcan XC 72R) powder was added in the DMF solution and mixed with dots. The CQD-carbon-powder mixture was precipitated via the addition of toluene and was separated by centrifugation. After the supernatant was removed, 3 mL of DMF was added again to the CQDs, which were then centrifuged for the removal of precursor residues. The left CQD-carbon-powder mixture was dried overnight in a vacuum chamber.

Preparation of QDDCs

After the CQD-carbon-powder mixture dried, active QDDCs were formed *in situ* in CO_2-saturated 0.5 M $KHCO_3$ reduction electrolyte with a standard three-electrode cell system. Typically, 4 mg of the CQD-carbon-powder mixture was dispersed in a 1 mL mixture of water and ethanol (4:1, v/v), and then 80 μL of Nafion solution (5 wt % in water) was added. We immersed the suspension in an ultrasonic bath for 30 min to prepare a homogeneous ink. We prepared the working electrode by depositing 10 μL (around 0.04 mg) catalyst ink onto carbon paper (Toray H060, Fuel Cell Store), the back of which we covered with kapton tape to avoid the competitive hydrogen evolution reaction on the carbon paper. After that, we fully reduced the electrode at a setting potential for 2 h to get the active QDDCs.

Preparation of Pb NPs

To synthesize monodisperse Pb NPs, we loaded 1.5 mmol lead(II) acetate and 7.5 mmol trioctylphosphine oxide into a 100 mL flask with 20 mL oleylamine and 20 mL octadecene. The above solution was dried under vacuum at 110°C for 1 h. The transparent solution was then rapidly heated to 200°C under N_2 flow. 10 min later, the reaction mixture was cooled down. After reaction, the aggregated NPs were separated by centrifugation. The supernatant was discarded, and the precipitate was redispersed in hexane. We repeated the washing procedure twice to remove the unreacted precursors. The obtained Pb NPs were then mixed with carbon (Vulcan XC 72R) powder and dried overnight in a vacuum chamber.

Preparation of Au NPs

Au NPs were prepared as follows: $HAuCl_4 \cdot 3H_2O$ (0.118 g dissolved in 5 mL H_2O) and tetraoctylammonium bromide (TOAB) (0.190 g dissolved in 10 mL toluene) were combined in a tri-neck round-bottom flask. After the solution was vigorously stirred for about 15 min, Au(III) was completely transferred to the toluene phase. 0.235 g triphenylphosphine (PPh_3) was added to the toluene solution under vigorous stirring. Then, $NaBH_4$ (0.034 g dissolved in 5 mL ethanol) was injected all at once. The reaction was allowed to proceed for 2 h at room temperature under air environment. A black product was obtained. The black product was washed several times with water and hexane for the removal of PPh_3 and TOAB.[51] The obtained Au NPs were then mixed with carbon (Vulcan XC 72R) powder and dried overnight in a vacuum chamber.

Please cite this article in press as: Liu et al., Quantum-Dot-Derived Catalysts for CO_2 Reduction Reaction, Joule (2019), https://doi.org/10.1016/j.joule.2019.05.010

Preparation of Electrodes

Typically, 4 mg of sample and carbon powder (weight ratio 1:1) was dispersed in a 1 mL mixture of water and ethanol (4:1,v/v), and then 80 μL of Nafion solution (5 wt % in water) was added. We immersed the suspension in an ultrasonic bath for 30 min to prepare a homogeneous ink. We prepared the working electrode by depositing 10 μL (around 0.04 mg) catalyst ink onto carbon paper (Toray H060, Fuel Cell Store), the back of which we covered with kapton tape to avoid the competitive hydrogen evolution reaction on the carbon paper.

Characterization

TEM, high-resolution TEM (HRTEM), and HAADF-STEM before and after CO_2RR were performed on a Hitachi 2700C and HF-3300 transmission electron microscope operated at 200 kV. We prepared the samples by dropping the catalyst powder dispersed in ethanol onto carbon-coated Cu TEM grids (Ted Pella) with micropipettes and dried them under ambient conditions. Powder X-ray diffraction (XRD) patterns were obtained with a MiniFlex600 instrument. Data were collected in Bragg-Brettano mode with 0.02° divergence and a scan rate of 0.1°/s. The specific surface areas of the samples were determined from the nitrogen absorption data at liquid nitrogen temperature according to the BET technique. The samples were degassed at 200°C and a pressure below 100 mTorr for a minimum of 2 h prior to analysis with a Micromeritics VacPrep 061 instrument. The total surface areas were deduced from the isotherm analysis in the relative pressure range from 0.05 to 0.20. The surface analysis was studied by XPS (model 5600, Perkin-Elmer). The binding energy data were calibrated with reference to the C 1s signal at 284.5 eV. Raman measurement was performed on a confocal micro-Raman spectrometer (Horiba Aramis) equipped with a 473 nm laser as the excitation source. The laser beam was focused with a ×50 long-working distance objective with a numeric aperture of 0.5, and the spot size was about 1.5 mm.

Electrochemical Measurements

All CO_2 reduction experiments were performed with a three-electrode system connected to an electrochemical workstation (Autolab PGSTAT302N) with a built-in EIS analyzer. QDDCs on carbon paper or a glassy carbon electrode were used as the working electrode. Ag/AgCl (with 3M KCl as the filling solution) and platinum mesh were used as reference and counter electrodes, respectively. Electrode potentials were converted to the RHE reference scale as follows: $E_{RHE} = E_{Ag/AgCl} + 0.197\ V + 0.0591 \times pH$. The electrolyte was 0.5 M $KHCO_3$ saturated with CO_2 with pH of 7.2. The experiments were performed in a gas-tight two-compartment H-cell separated by an ion-exchange membrane (Nafion117). The electrolyte in the cathodic compartment was stirred at a rate of 300 rpm during electrolysis. CO_2 gas was delivered into the cathodic compartment at a rate of 5.00 standard cubic centimeters per minute (s.c.c.m.) and was routed into a gas chromatograph (PerkinElmer Clarus 600). The liquid products were quantified by NMR (Agilent DD2-500) spectroscopy, for which 0.5 mL electrolyte was mixed with 0.1 mL D_2O (deuterated water), and 0.05 μL dimethyl sulfoxide (Sigma, 99.99%) was added as an internal standard. The one-dimensional ^1H spectrum was measured with water suppressios by a pre-saturation method. The FE of formate was calculated from the total amount of charge Q (in coulombs) passed through the sample and the total amount of formate produced ($n_{formate}$, in moles). $Q = I \times t$, where I (in amperes) is the reduction current at a specific applied potential and t is the time (in seconds) for the constant reduction current. The total amount of formate produced was measured by NMR (Agilent DD2-500) spectroscopy. Assuming that two electrons

Please cite this article in press as: Liu et al., Quantum-Dot-Derived Catalysts for CO_2 Reduction Reaction, Joule (2019), https://doi.org/10.1016/j.joule.2019.05.010

are needed to produce one formate molecule, the FE can be calculated as follows:[5] FE = $2F \times n_{formate}/Q = 2F \times n_{formate}/(I \times t)$, where F is the Faraday constant.

The electrochemical active surface area (ECSA) was measured by the underpotential-deposited method.[1] The electrode was immersed in a 0.50 M H_2SO_4 solution containing 100 mM $CuSO_4$ continuously purged with N_2. Cyclic voltammograms (CVs) from 0.83 to 0.483 V (versus Ag/AgCl) at a scan rate of 50 mV s^{-1} were acquired repeatedly until traces converged. The anodic stripping waves at 0.39 V versus Ag/AgCl were integrated. The factor used to convert the stripping charge to surface area was 92.4 μC cm^{-2}. To accurately detect the ECSA, we also integrated the reduction peak area obtained from CVs in the 50 mM H_2SO_4[52] with a scan rate of 10 mV s^{-1}. In the forward scan, a monolayer of chemisorbed oxygen was formed, and then it was reduced in the reverse scan. We calculated the surface area by integrating the reduction peak (0.9 V versus Ag/AgCl) to obtain the reduction charge. The reduction charge per microscopic unit area was experimentally determined to be 448 μC/cm^2. The error of the results obtained from these two methods is within 5%, indicating an accurate estimation of ECSA.

For temperature-dependent measurements, the sealed glass cell was suspended in a thermostatic silicone oil bath. The electrodes were passed through holes in the lid with an O-ring slightly larger than the electrodes to minimize evaporative losses. The effect of temperature on the performance of the catalysts is shown in Figure S42. As expected, the kinetics of the CO_2RR were increased at elevated temperatures, reflecting the temperature dependence of the chemical rate constant, which is approximately proportional to $\exp(-\Delta H^*/kT)$, where ΔH^* is the apparent enthalpy of activation (hereafter termed the activation energy), and k is the Boltzmann constant. Specifically, the apparent electrochemical activation energy (ΔH^*) for CO_2RR can be determined according to the Arrhenius relationship:[37,53,54]

$$\frac{\partial(\log i_k)}{\partial(1/T)}\Big|_v = \frac{\Delta H^*}{2.3},$$

where i_k is the kinetic current at $\nu = -400$ mV, T is the temperature, and R is the universal gas constant.

In Situ XAS Measurement

In situ XAS measurements were conducted at Taiwan Beam Lines BL01C1, BL07A1, and BL17C1 at the National Synchrotron Radiation Research Center (Hsinchu, Taiwan). The electron-storage ring was operated at 1.5 GeV with a current of 300 mA. A Si (111) double-crystal monochromator was employed for the energy selection with resolution dE/E better than 2×10^{-4} at different element (M: Pb, Au, Ag, and Cu) L_3- or K-edges. The measurement on metal NPs was performed in a purpose-made stainless-steel cell for the H_2-atmosphere reduction treatment. The *in situ* measurements on QDDCs NPs were conducted in a self-designed three-electrode electrochemical cell through electrochemical reducing metal sulfide CQDs in CO_2-saturated $KHCO_3$ solutions at −0.2 V different potentials. All XAS spectra were recorded at room temperature in transmission mode. Higher harmonics were eliminated through detuning of the double-crystal Si (111) monochromator. Three gas-filled ionization chambers were used in series for measuring the intensities of the incident beam (I_o), the beam transmitted by the sample (I_t), and the beam subsequently transmitted by the reference foil (I_{re}). The third ion chamber was used in conjunction with the reference metal foil for element L_3- or K- edge measurements. All measurements were compared against the reference samples. Control of parameters for EXAFS measurements, collection modes, data processing, and error calculation were performed according to the guidelines set by the Standards and Criteria Committee of the International XAFS Society.[55]

Ex Situ XAS Measurement

The *ex situ* Pb L_3-edge and S K-edge XAS data were collected on Sector 20-BM at the Advanced Photon Source and Soft X-Ray Microcharacterization Beamline at the Canadian Light Source, respectively. Pb L_3-edge and S K-edge XANES spectra were recorded at 12.9–13.2 keV and 2.45–2.55 keV, respectively, in fluorescence mode with a step size of 0.6 and 0.25 eV at the near edge, respectively. All samples for *ex situ* measurements were prepared on carbon paper and Kapton tapes after CO_2RR.

XAS Data Analyses

We obtained the EXAFS function, χ, by subtracting the post-edge background from the overall absorption coefficient and then normalizing to the edge jump. The normalized function, $\chi(E)$, was then converted to k space, which is the photoelectron wave vector. We weighted the wave-vector function $\chi(k^n)$ by k^n to compensate for the damping of the backscattering oscillation in the high k region. Subsequently, we converted k^n-weighted $\chi(k^n)$ data ranging from $\sim$3 to $\sim$10 Å^{-1} at various elements L_3- or K-edge to r space by Fourier transformation to identify the backscattering contributions of each coordination shell. A nonlinear least-squares algorithm was employed to curve fitting in the r space range. The reference phase and amplitude of M-M absorber were obtained from corresponding metal foil. All computer programs were implemented in the UWXAFS 3.0 package,[56] and the backscattering amplitude and phase shift of the specific-atom model were calculated by the FEFF8 code.[57] In this analysis, the structural parameters corresponding to first-shell coordination, such as CNs (N), bond length (R), the Debye-Waller factor (σ_j^2), and inner potential shift (ΔE_0), were calculated. The amplitude reduction factor (S_0^2) represents the energy loss during multiple electron excitations. Fixing the CN values in the FEFFIT input file yielded a S_0^2 value near 0.95 for various elements.

SUPPLEMENTAL INFORMATION

Supplemental Information can be found online at https://doi.org/10.1016/j.joule.2019.05.010.

ACKNOWLEDGMENTS

This work was supported financially by the National Natural Science Foundation of China (21872174), International S&T Cooperation Program of China (2017YFE0127800), the Ontario Research Fund Research-Excellence Program, the Natural Sciences and Engineering Research Council (NSERC) of Canada, the Canadian Institute for Advanced Research Bio-inspired Solar Energy program, a University of Toronto Connaught grant, the Ministry of Science and Technology of Taiwan, the King Abdullah University of Science and Technology (KAUST), the Project of Innovation-Driven Plan in Central South University (2017CX003, 20180018050001), the Hunan Provincial Science and Technology Program (2017XK2026), the State Key Laboratory of Powder Metallurgy in Central South University, the Shenzhen Science and Technology Innovation Project (JCYJ20180307151313532, JCYJ20180307164633296), the Thousand Youth Talents Plan of China, and the Hundred Youth Talents Program of Hunan. S.M.K., Z.C., and L.C. thank the KAUST Supercomputing Laboratory for the resources provided. This work benefited from Taiwan Beam Lines BL01C1, BL07A1, and BL17C1 in the National Synchrotron Radiation Research Center, the Soft X-Ray Microcharacterization Beamline at Canadian Light Source (CLS) and Sector 20-BM at the Advanced Photon Source (APS).

Please cite this article in press as: Liu et al., Quantum-Dot-Derived Catalysts for CO_2 Reduction Reaction, Joule (2019), https://doi.org/10.1016/j.joule.2019.05.010

The authors thank Y. Pang, J. Fan, O.Voznyy, J. Xu, F. Arquer, T. Safaei, A. Klinkova, R. Wolowiec, D. Kopilovic, L. Levina, J. Tam, S. Boccia, and S. Hoogland from U of T for fruitful discussions; Y. Hu from CLS; Z. Finfrock and M. Ward from APS; and C. Xiao from the University of Science and Technology of China for their help during the study.

AUTHOR CONTRIBUTIONS

Min Liu, E.H.S., and B.-J.H. supervised the project. Min Liu, Mengxia Liu, and X.W. designed the experiments. S.M.K., Z.C., and L.C. carried out electrochemical simulations. S.M.K., Z.C., and L.C. carried out electrochemical simulations. P.D.L. and A.S. carried out simulations of vacancy formation energies. Mengxia Liu, X.L., P.W., and H.L. synthesized quantum dots and did ligand exchange. Min Liu, X.W., Z.W., T.-S.C., T.-K.S., and B.-J.H. performed the X-ray measurements. Y.Y. carried out *in situ* Raman measurements. D.Z. and Y.H. performed the TEM measurements. H.L. and K.L. carried out the XPS measurements. X.Q., J.H, C.J., H.Z., M.Z., Y.Z., C.T.D., and C.Z. performed electrochemical measurements. All authors discussed the results and assisted during manuscript preparation.

DECLARATION OF INTERESTS

The authors declare no competing interests.

Received: January 29, 2019
Revised: March 16, 2019
Accepted: May 9, 2019
Published: June 25, 2019

REFERENCES

1. Liu, M., Pang, Y., Zhang, B., De Luna, P., Voznyy, O., Xu, J., Zheng, X., Dinh, C.T., Fan, F., Cao, C., et al. (2016). Enhanced electrocatalytic CO_2 reduction via field-induced reagent concentration. Nature *537*, 382–386.
2. Luo, J., Im, J.H., Mayer, M.T., Schreier, M., Nazeeruddin, M.K., Park, N.G., Tilley, S.D., Fan, H.J., and Grätzel, M. (2014). Water photolysis at 12.3% efficiency via perovskite photovoltaics and Earth-abundant catalysts. Science *345*, 1593–1596.
3. Mariano, R.G., McKelvey, K., White, H.S., and Kanan, M.W. (2017). Selective increase in CO_2 electroreduction activity at grain-boundary surface terminations. Science *358*, 1187–1192.
4. Li, C.W., Ciston, J., and Kanan, M.W. (2014). Electroreduction of carbon monoxide to liquid fuel on oxide-derived nanocrystalline copper. Nature *508*, 504–507.
5. Gao, S., Lin, Y., Jiao, X., Sun, Y., Luo, Q., Zhang, W., Li, D., Yang, J., and Xie, Y. (2016). Partially oxidized atomic cobalt layers for carbon dioxide electroreduction to liquid fuel. Nature *529*, 68–71.
6. Dinh, C.-T., Burdyny, T., Kibria, M.G., Seifitokaldani, A., Gabardo, C.M., García de Arquer, F.P., Kiani, A., Edwards, J.P., De Luna, P., Bushuyev, O.S., et al. (2018). CO_2 electroreduction to ethylene via hydroxide-mediated copper catalysis at an abrupt interface. Science *360*, 783–787.
7. Zhou, Y., Che, F., Liu, M., Zou, C., Liang, Z., De Luna, P., Yuan, H., Li, J., Wang, Z., Xie, H., et al. (2018). Dopant-induced electron localization drives CO_2 reduction to C_2 hydrocarbons. Nat. Chem. *10*, 974–980.
8. De Luna, P., Quintero-Bermudez, R., Dinh, C.-T., Ross, M.B., Bushuyev, O.S., Todorović, P., Regier, T., Kelley, S.O., Yang, P., and Sargent, E.H. (2018). Catalyst electro-redeposition controls morphology and oxidation state for selective carbon dioxide reduction. Nat. Catal. *1*, 103–110.
9. Zhu, W., Zhang, Y.J., Zhang, H., Lv, H., Li, Q., Michalsky, R., Peterson, A.A., and Sun, S. (2014). Active and selective conversion of CO_2 to CO on ultrathin Au nanowires. J. Am. Chem. Soc. *136*, 16132–16135.
10. Lu, Q., Rosen, J., Zhou, Y., Hutchings, G.S., Kimmel, Y.C., Chen, J.G., and Jiao, F. (2014). A selective and efficient electrocatalyst for carbon dioxide reduction. Nat. Commun. *5*, 3242.
11. Zhu, W., Michalsky, R., Metin, Ö., Lv, H., Guo, S., Wright, C.J., Sun, X., Peterson, A.A., and Sun, S. (2013). Monodisperse Au nanoparticles for selective electrocatalytic reduction of CO_2 to CO. J. Am. Chem. Soc. *135*, 16833–16836.
12. Chen, Y., Li, C.W., and Kanan, M.W. (2012). Aqueous CO_2 reduction at very low overpotential on oxide-derived Au nanoparticles. J. Am. Chem. Soc. *134*, 19969–19972.
13. Mistry, H., Varela, A.S., Bonifacio, C.S., Zegkinoglou, I., Sinev, I., Choi, Y.W., Kisslinger, K., Stach, E.A., Yang, J.C., Strasser, P., and Cuenya, B.R. (2016). Highly selective plasma-activated copper catalysts for carbon dioxide reduction to ethylene. Nat. Commun. *7*, 12123.
14. Lin, S., Diercks, C.S., Zhang, Y.B., Kornienko, N., Nichols, E.M., Zhao, Y., Paris, A.R., Kim, D., Yang, P., Yaghi, O.M., and Chang, C.J. (2015). Covalent organic frameworks comprising cobalt porphyrins for catalytic CO_2 reduction in water. Science *349*, 1208–1213.
15. Kim, D., Xie, C., Becknell, N., Yu, Y., Karamad, M., Chan, K., Crumlin, E.J., Nørskov, J.K., and Yang, P. (2017). Electrochemical activation of CO_2 through atomic ordering transformations of AuCu nanoparticles. J. Am. Chem. Soc. *139*, 8329–8336.
16. Kim, D., Resasco, J., Yu, Y., Asiri, A.M., and Yang, P. (2014). Synergistic geometric and electronic effects for electrochemical reduction of carbon dioxide using gold-copper bimetallic nanoparticles. Nat. Commun. *5*, 4948.
17. Liu, M., Voznyy, O., Sabatini, R., García de Arquer, F.P., Munir, R., Balawi, A.H., Lan, X., Fan, F., Walters, G., Kirmani, A.R., et al. (2017). Hybrid organic-inorganic inks flatten the energy landscape in colloidal quantum dot solids. Nat. Mater. *16*, 258–263.
18. Ning, Z., Voznyy, O., Pan, J., Hoogland, S., Adinolfi, V., Xu, J., Li, M., Kirmani, A.R., Sun, J.P., Minor, J., et al. (2014). Air-stable n-type colloidal quantum dot solids. Nat. Mater. *13*, 822–828.
19. Tang, J., Kemp, K.W., Hoogland, S., Jeong, K.S., Liu, H., Levina, L., Furukawa, M., Wang, X.,

Please cite this article in press as: Liu et al., Quantum-Dot-Derived Catalysts for CO_2 Reduction Reaction, Joule (2019), https://doi.org/10.1016/j.joule.2019.05.010

Debnath, R., Cha, D., et al. (2011). Colloidal-quantum-dot photovoltaics using atomic-ligand passivation. Nat. Mater. *10*, 765–771.

20. Fan, F., Voznyy, O., Sabatini, R.P., Bicanic, K.T., Adachi, M.M., McBride, J.R., Reid, K.R., Park, Y.S., Li, X., Jain, A., et al. (2017). Continuous-wave lasing in colloidal quantum dot solids enabled by facet-selective epitaxy. Nature *544*, 75–79.

21. Hammer, B., and Nørskov, J.K. (2000). Adv. Catal. *45*, 71–129.

22. Jiao, Y., Du, A., Zhu, Z., Rudolph, V., Lu, G.Q., and Smith, S.C. (2011). A density functional theory study on CO_2 capture and activation by graphene-like boron nitride with boron vacancy. Catal. Today *175*, 271–275.

23. Li, H., Tsai, C., Koh, A.L., Cai, L., Contryman, A.W., Fragapane, A.H., Zhao, J., Han, H.S., Manoharan, H.C., Abild-Pedersen, F., et al. (2016). Activating and optimizing MoS_2 basal planes for hydrogen evolution through the formation of strained sulphur vacancies. Nat. Mater. *15*, 48–53.

24. Swaminathan, J., Subbiah, R., and Singaram, V. (2016). Defect-rich metallic titania ($TiO_{1.23}$)—an efficient hydrogen evolution catalyst for electrochemical water splitting. ACS Catal. *6*, 2222–2229.

25. Zhao, Y., Chen, G., Bian, T., Zhou, C., Waterhouse, G.I., Wu, L.Z., Tung, C.H., Smith, L.J., O'Hare, D., and Zhang, T. (2015). Defect-rich ultrathin ZnAl-layered double hydroxide nanosheets for efficient photoreduction of CO_2 to CO with water. Adv. Mater. *27*, 7824–7831.

26. Dubau, L., Nelayah, J., Moldovan, S., Ersen, O., Bordet, P., Drnec, J., Asset, T., Chattot, R., and Maillard, F. (2016). Defects do catalysis: CO monolayer oxidation and oxygen reduction reaction on hollow PtNi/C nanoparticles. ACS Catal. *6*, 4673–4684.

27. Wang, H., Xu, S., Tsai, C., Li, Y., Liu, C., Zhao, J., Liu, Y., Yuan, H., Abild-Pedersen, F., Prinz, F.B., et al. (2016). Direct and continuous strain control of catalysts with tunable battery electrode materials. Science *354*, 1031–1036.

28. Apai, G., Hamilton, J.F., Stohr, J., and Thompso, A. (1979). n, extended X-ray absorption fine structure of small Cu and Ni clusters: binding-energy and bond-length changes with cluster size. Phys. Rev. Lett. *43*, 165–169.

29. Miller, J.T., Kropf, A.J., Zha, Y., Regalbuto, J.R., Delannoy, L., Louis, C., Bus, E., and van Bokhoven, J.A. (2006). The effect of gold particle size on AuAu bond length and reactivity toward oxygen in supported catalysts. J. Catal. *240*, 222–234.

30. Van Grieken, R., and Markowicz, A. (2001). Handbook of X-Ray Spectrometry (CRC Press).

31. Lee, C.H., and Kanan, M.W. (2015). Controlling H+ vs CO_2 reduction selectivity on Pb electrodes. ACS Catal. *5*, 465–469.

32. Kwon, Y., and Lee, J. (2010). Formic acid from carbon dioxide on nanolayered electrocatalyst. Electrocatalysis *1*, 108–115.

33. Klinkova, A., De Luna, P., Dinh, C.-T., Voznyy, O., Larin, E.M., Kumacheva, E., and Sargent, E.H. (2016). Rational design of efficient palladium catalysts for electroreduction of carbon dioxide to formate. ACS Catal. *6*, 8115–8120.

34. Min, X., and Kanan, M.W. (2015). Pd-catalyzed electrohydrogenation of carbon dioxide to formate: high mass activity at low overpotential and identification of the deactivation pathway. J. Am. Chem. Soc. *137*, 4701–4708.

35. Back, S., Yeom, M.S., and Jung, Y. (2015). Active sites of Au and Ag nanoparticle catalysts for CO_2 electroreduction to CO. ACS Catal. *5*, 5089–5096.

36. Zhang, B., Zheng, X., Voznyy, O., Comin, R., Bajdich, M., García-Melchor, M., Han, L., Xu, J., Liu, M., Zheng, L., et al. (2016). Homogeneously dispersed multimetal oxygen-evolving catalysts. Science *352*, 333–337.

37. Morris, A.J., McGibbon, R.T., and Bocarsly, A.B. (2011). Electrocatalytic carbon dioxide activation: the rate-determining step of pyridinium-catalyzed CO_2 reduction. ChemSusChem *4*, 191–196.

38. Innocent, B., Liaigre, D., Pasquier, D., Ropital, F., Léger, J.-M., and Kokoh, K.B. (2008). Electro-reduction of carbon dioxide to formate on lead electrode in aqueous medium. J. Appl. Electrochem. *39*, 227–232.

39. Kresse, G., and Furthmüller, J. (1996). Efficient iterative schemes for ab initio total-energy calculations using a plane-wave basis set. Phys. Rev. B Condens. Matter *54*, 11169–11186.

40. Perdew, J.P., Burke, K., and Ernzerhof, M. (1996). Generalized gradient approximation made simple. Phys. Rev. Lett. *77*, 3865–3868.

41. Grimme, S., Antony, J., Ehrlich, S., and Krieg, H. (2010). A consistent and accurate ab initio parametrization of density functional dispersion correction (DFT-D) for the 94 elements H-Pu. J. Chem. Phys. *132*, 154104.

42. Kresse, G., and Joubert, D. (1999). From ultrasoft pseudopotentials to the projector augmented-wave method. Phys. Rev. B *59*, 1758–1775.

43. Jain, A., Ong, S.P., Hautier, G., Chen, W., Richards, W.D., Dacek, S., Cholia, S., Gunter, D., Skinner, D., Ceder, G., and Persson, K.A. (2013). Commentary: The Materials Project: a materials genome approach to accelerating materials innovation. APL Mater. *1*, 011002.

44. Peterson, A.A., Abild-Pedersen, F., Studt, F., Rossmeisl, J., and Norskov, J.K. (2010). How copper catalyzes the electroreduction of carbon dioxide into hydrocarbon fuels. Energy Environ. Sci. *3*, 1311–1315.

45. Nørskov, J.K., Rossmeisl, J., Logadottir, A., and Lindqvist, L. (2004). Origin of the overpotential for oxygen reduction at a fuel-cell cathode. J. Phys. Chem. B *108*, 17886–17892.

46. Christensen, R., Hansen, H.A., and Vegge, T. (2015). Identifying systematic DFT errors in catalytic reactions. Catal. Sci. Technol. *5*, 4946–4949.

47. Ning, Z., Zhitomirsky, D., Adinolfi, V., Sutherland, B., Xu, J., Voznyy, O., Maraghechi, P., Lan, X., Hoogland, S., Ren, Y., and Sargent, E.H. (2013). Graded doping for enhanced colloidal quantum dot photovoltaics. Adv. Mater. *25*, 1719–1723.

48. Luther, J.M., Jain, P.K., Ewers, T., and Alivisatos, A.P. (2011). Localized surface plasmon resonances arising from free carriers in doped quantum dots. Nat. Mater. *10*, 361–366.

49. Tang, R., Xue, J., Xu, B., Shen, D., Sudlow, G.P., and Achilefu, S. (2015). Tunable ultrasmall visible-to-extended near-infrared emitting silver sulfide quantum dots for integrin-targeted cancer imaging. ACS Nano *9*, 220–230.

50. Kristl, M., and Drofenik, M. (2003). Preparation of Au_2S_3 and nanocrystalline gold by sonochemical method. Inorg. Chem. Commun. *6*, 1419–1422.

51. Qian, H., Zhu, M., Lanni, E., Zhu, Y., Bier, M.E., and Jin, R. (2009). Conversion of polydisperse Au nanoparticles into monodisperse Au_{25} nanorods and nanospheres. J. Phys. Chem. C *113*, 17599–17603.

52. Bin, X., Sargent, E.H., and Kelley, S.O. (2010). Nanostructuring of sensors determines the efficiency of biomolecular capture. Anal. Chem. *82*, 5928–5931.

53. Ghuman, K.K., Wood, T.E., Hoch, L.B., Mims, C.A., Ozin, G.A., and Singh, C.V. (2015). Illuminating CO_2 reduction on frustrated Lewis pair surfaces: investigating the role of surface hydroxides and oxygen vacancies on nanocrystalline $In_2O_{(3-x)}(OH)_y$. Phys. Chem. Chem. Phys. *17*, 14623–14635.

54. Schmeier, T.J., Dobereiner, G.E., Crabtree, R.H., and Hazari, N. (2011). Secondary coordination sphere interactions facilitate the insertion step in an iridium(III) CO_2 reduction catalyst. J. Am. Chem. Soc. *133*, 9274–9277.

55. Sayers, D.E. (2000). Report of the International XAFS Society Standards and Criteria Committee. http://ixs.iit.edu/subcommittee_reports/sc/SC00report.pdf.

56. Stern, E.A., Newville, M., Ravel, B., Yacoby, Y., and Haskel, D. (1995). The UWXAFS analysis package: philosophy and details. Physica B *208*, 117–120.

57. Zabinsky, S.I., Rehr, J.J., Ankudinov, A., Albers, R.C., and Eller, M.J. (1995). Multiple-scattering calculations of X-ray-absorption spectra. Phys. Rev. B Condens. Matter *52*, 2995–3009.